Supplement of The Cryosphere, 19, 541–563, 2025
https://doi.org/10.5194/tc-19-541-2025-supplement

The Cryosphere Open Access EGU

Supplement of

ISMIP6-based Antarctic projections to 2100: simulations with the BISICLES ice sheet model

James F. O'Neill et al.

Correspondence to: James F. O'Neill (j.oneill2@exeter.ac.uk)

S1 Supplementary Document

In the following we present supplementary information describing BISICLES ice sheet model equations and details of the adaptive mesh grid. We include additional discussion of our control simulation and relaxation simulation. We present thickness change for all projection experiments (i.e. not including the control). Finally, we provide a table of masked model results referenced in the main text.

S1 BISICLES model equations

BISICLES implements the L1L2 approximation of the Stokes model on a block structured grid with adaptive mesh refinement (Cornford et al., 2013). BISICLES assumes that ice is in hydrostatic equilibrium, such that given bedrock elevation b, and ice thickness h, the surface elevation of the ice sheet s, is given by:

$$s = \max\left[h + b, \left(1 - \frac{\rho_i}{\rho_w}\right) h\right], \tag{S1}$$

where ρ_i is the density of ice and ρ_w is the density of sea water (Cornford et al., 2015).

Horizontal velocity $\boldsymbol{u}$ and thickness (h) satisfy a mass conservation equation for depth-integrated transport of an incompressible material:

$$\frac{\delta h}{\delta t} + \nabla \cdot [\boldsymbol{u} h] = M_s - M_b, \tag{S2}$$

where M_s is the meteoric accumulation rate i.e. due to surface mass balance processes, and M_b is the basal melt rate applied to the underside of ice shelves in cells with a centre at floatation. Incompressible (shear-thinning) flow of ice under gravity satisfies a stress balance equation:

$$\nabla \cdot [\phi h \mu (2\dot{\epsilon} + 2tr(\dot{\epsilon})\mathbf{I}] + \boldsymbol{\tau_b} = \rho_i g h \nabla s, \tag{S3}$$

where $\mathbf{I}$ is the identity tensor and g is acceleration due to gravity, and $tr(\dot{\epsilon})$ indicates the trace of $\dot{\epsilon}$. The strain rate tensor, $\dot{\epsilon}$, is given by:

$$\dot{\epsilon} = \frac{1}{2}[\nabla \boldsymbol{u} + (\nabla \boldsymbol{u})^T]. \tag{S4}$$

The term $\phi h \mu$ in Equation S3 is the vertically-integrated effective viscosity. ϕ is a stiffening factor, which represents changes to ice viscosity due to factors such as temperature and crevasse weakening. For modern ice sheet studies, ϕ is found by inversion and tuned to match observations (e.g. Cornford et al. 2015). The effect of vertical shear strain is retained through viscosity, μ, which satisfies the below equation when the exponent n=3 in Glen's flow law (see Cornford et al. (2015)):

$$2\mu A(T)(4\mu^2\dot{\epsilon}^2 + |\rho_i g(s-z)\nabla s|^2) = 1, \tag{S5}$$

where $A(T)$ is a rate factor that depends on temperature through the Arrhenius Law described by Hooke (1981), s is the surface and z is depth in the ice sheet.

Our experiments in this study use the two-component sliding law of Tsai et al. (2015):

$$\tau_b = min[C(\boldsymbol{u}_b)^{(\frac{1}{m})}, C_f N] \tag{S6}$$

The two component basal sliding law facilitates Coulomb type sliding where saturated till at the base of the ice sheet, or water filled cavities, enable plastic sliding. For hard beds under the Tsai friction law, Weertman sliding is used.

S2 BISICLES model grid

BISICLES uses adaptive mesh refinement, with a base horizontal resolution of 8 km and finest resolution of 1 km in the simulations presented in this study. The model mesh is updated as the model evolves, so it is not fixed and differs between experiments. Figure S1 shows an example of the BISICLES mesh at a time slice for the control simulation, to illustrate how the mesh is structured.

S3 BISICLES relaxation simulation

As outlined in the Methods section of the main text, following the inversion for basal sliding parameters and ϕ, we run a relaxation simulation of ~9 years. This allows the velocity and thickness fields to adjust to remove spurious variations in

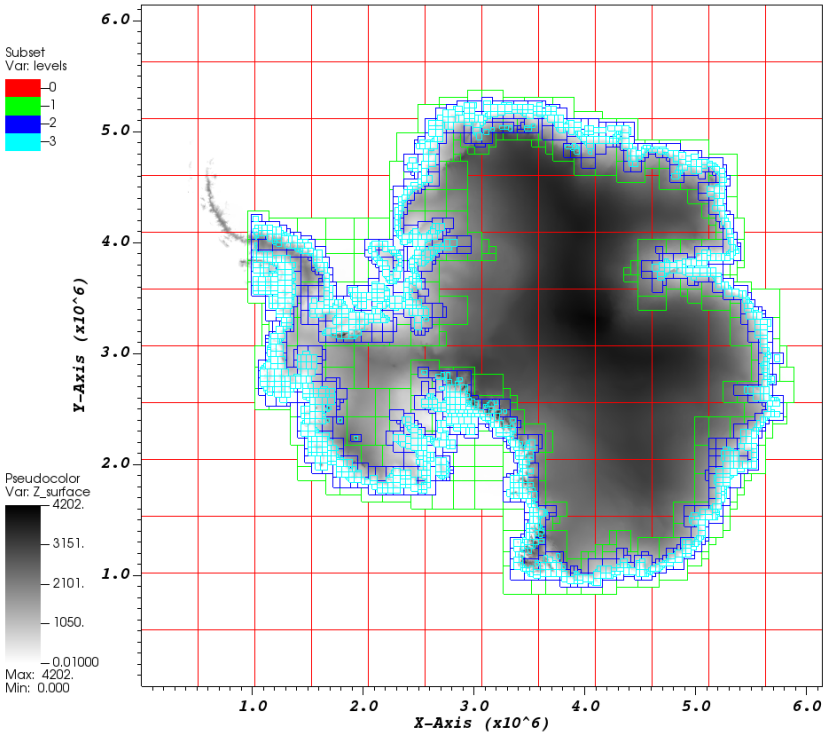

Fig. S1. Example of BISICLES mesh refinement for an example time slice in the control simulation. Within the red boxes, resolution is 8 km, green boxes bound regions with 1 level of refinement to 4 km, dark blue boxes bound regions with 2 levels of refinement to 2 km and light blue boxes bound regions with 3 levels of refinement and 1 km resolution. Shown in grey is the ice sheet surface elevation ('Z_surface', m.a.s.l)

thickening rate, that can for example arise from the fact that the velocity observations and thickness data were not collected concurrently (Cornford et al., 2015). Figure S2 shows ice sheet thickness (Fig. S2a) and speed (Fig. S2b) at the end of the relaxation period. Figure S2c shows the thickness change over the ~9 year relaxation simulation. The majority of thinning occurs around the margins of the grounded ice sheet. Figure S2d shows speed change over the relaxation simulation. Speed-up is greatest around Thwaites and Pine Island glacier, with speed-up in East Antarctic ice streams extending less far upstream. Ice shelves predominantly slow down through the relaxation period. Figure S2e shows the observed Antarctic ice speed from Rignot et al. (2017), and Fig. S2f shows the difference between this and the speed at the end of our relaxation run i.e. the initial speed for projection simulations and the control. As shown in Fig. S2f, ice speed is generally lower for grounded ice than the observations, whilst floating ice speeds are greater. Overall however, compared with other ISMIP6 models initial velocity (Serroussi et al. (2019), Fig. 3), BISICLES has fairly good agreement with speed observations - with a root-mean-squared-

error (RMSE) of 72 m yr^{-1}. Similarly, whilst there is divergence from the initial Bedmap2 based ice sheet thickness in the relaxation simulation, RMSE compared with the original Bedmap2 data (Fretwell et al., 2013) is low compared with other models (Serroussi et al. (2019), Fig. 3). Comparing our initial thickness and Bedmap2 on a common 8 km grid, RMSE is 54 m. As noted in the main text, our initial condition generated at the end of the relaxation simulation is the same as that presented in InitMIP (Seroussi et al., 2019), where it is presented alongside other ISMIP6 models.

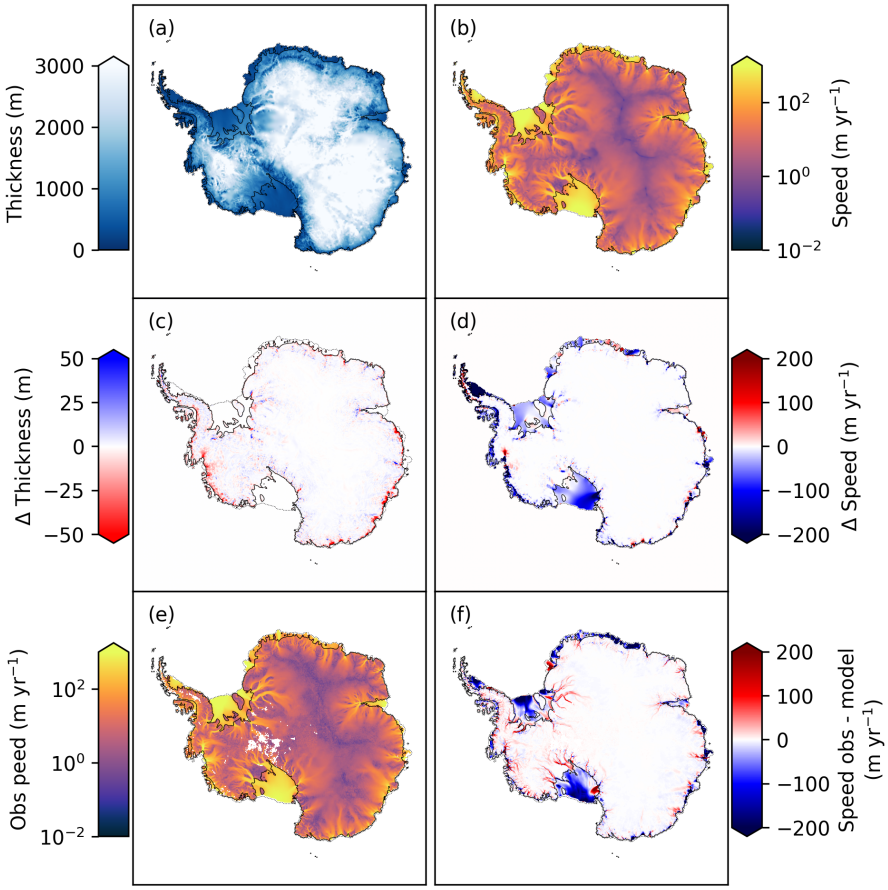

Fig. S2. Ice sheet thickness at the end of the relaxation simulation (**a**), which is the same as initial, 2010 thickness for our projection simulations. Ice speed at the end of the relaxation simulation (**b**), which is the same as initial, 2010 speed for projection simulations. Change in thickness over the course of the relaxation simulation (**c**). Change in speed over the course of the relaxation simulation (**d**). Observed speed from Rignot et al. (2017), regridded to 8 km resolution (**e**), with white regions showing missing data. Difference between observed speed and speed at the end of the relaxation simulation (**f**). Black solid contours show grounding line position at the end of the relaxation period. Black dashed line shows shelf position at the end of the relaxation period.

S4 Control simulation

As outlined in the main text, the control simulation uses the surface mass balance forcing of Arthern et al. (2006). Figure S3a shows this surface mass balance in kg m^{-2} yr^{-1}. The Arthern et al. (2006) based surface mass balance captures the broad patterns of low surface mass balance over the high, dry East Antarctic ice sheet, with higher surface mass balance over the Antarctic Peninsula and coastal regions. Surface mass balance over Antarctica remains uncertain, with few direct observations. A range of regional Antarctic surface mass balance products exist, and were explored in Mottram et al. (2021). Qualitative comparisons can be made with the ensemble mean surface mass balance from 1987 to 2015, as presented in Mottram et al. (2021), and the surface mass balance forcing used for our control experiment. Note that the color scale in Fig. S3a is the same as that used in Mottram et al. (2021), Figure 6a to aid comparison. Compared with average surface mass balance shown in Mottram et al. (2021, Figure 6a), our control forcing has higher surface mass balance over areas of East Antarctica, but is drier around coastal regions. However, Mottram et al.(2021) note large differences in modelled surface mass balance from different products. The integrated surface mass balance of 2,144 Gt yr^{-1} for the forcing used in our control is within the range of 1980-2010 climatological mean surface mass balance of 1,961±70 Gt yr^{-1} to 2,519±118 Gt yr^{-1} reported in Mottram et al. (2021), though below the ensemble mean of 2,483 Gt yr^{-1} across products. Our background basal melt rate, as used in the control simulation is shown in Fig. S3b, with basal melt for keys regions shown in Fig. S3d - g.

Our background basal melt forcing is calculated in such a way that it holds the ice shelves close to their present day geometry, but allows thinning due to advection, whilst maintaining high basal melt rates close to the grounding line. We can compare the basal melt rate used in the control simulation with the observation-based basal melt rates calculated by Adusumilli et al. (2020). Figure S4a shows this observation-based, average 2010 to 2018 basal melt rate (Adusumilli et al., 2020). Figure S4b subtracts the average 2015 to 2100 basal melt rate for our control (Fig. S3b) from the observation based melt rates of Adusumilli et al. (2020). For the interior of the major ice shelves (Fig. S4c and f), where basal melting is low in our simulations and the observations, there is fairly good agreement between the two. Similarly, for the ice shelves fringing Dronning Maud Land (Fig. S4g), our applied basal melt rate, averaged from 2015 to 2100, is similar to the observations. For the Amundsen Sea Embayment (Fig. S4e) and Totten glacier (Fig. S4d), there are larger discrepancies between our applied melt rates and those of Adusumilli et al. (2020). Though the sign and magnitude of difference varies, observed basal melt rates generally exceed those applied in our model.

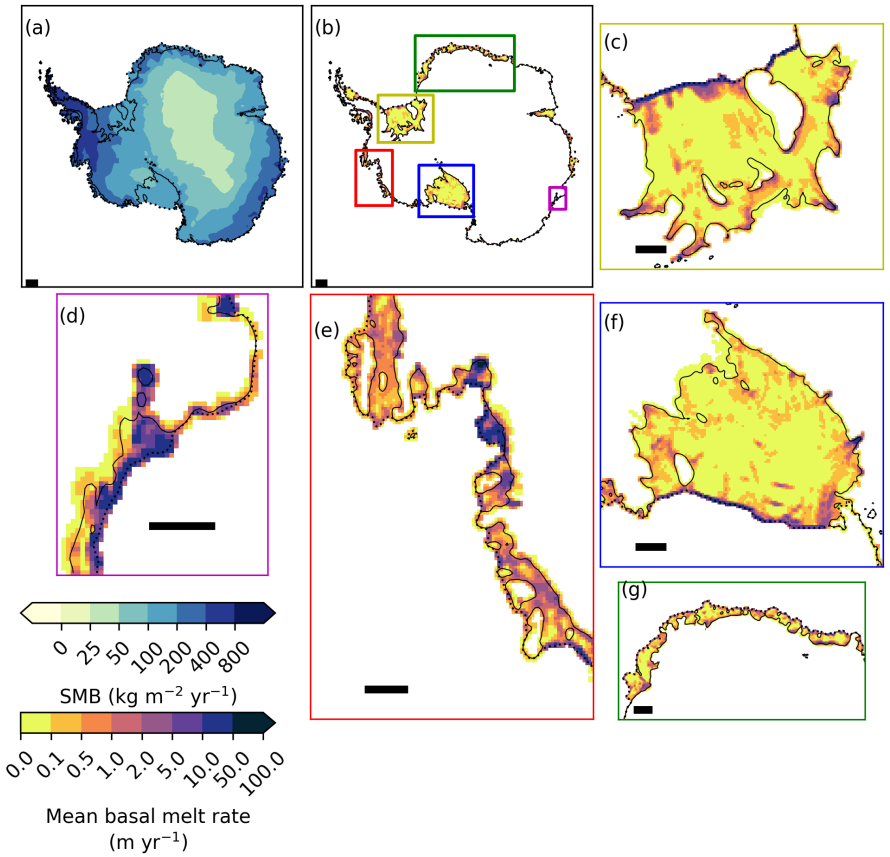

Fig. S3. Surface mass balance (SMB) (kg m^{-2} yr^{-1}) for the control experiment (**a**). Average basal melt rate (m yr^{-1}) from 2015 to 2100 for the control experiment for the whole domain (**b**). Also shown are zoomed in plots of basal melt rate for keys regions: the Filchner-Ronne ice shelf (**c**); the Totten glacier region (**d**); the Amundsen Sea Embayment (**e**); the Ross ice shelf (**f**) and Dronning Maud Land coast ice shelves (**g**). Bounding box colours for subplots **c** - **g** correspond to box locations outlined in **b**. Solid black contours on **a** - **g** show 2015 grounding line position, and dashed black contours show shelf edge. Black horizontal lines are scale bars corresponding to 100 km.

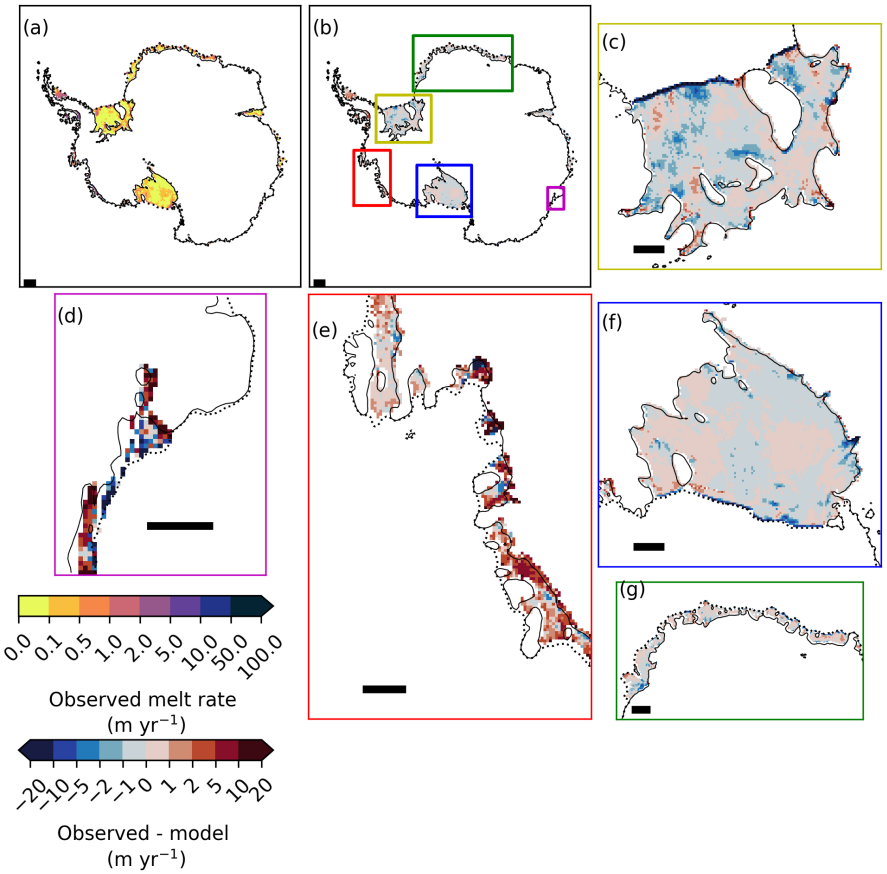

Fig. S4. Average 2010 to 2018 Antarctic basal melt rate (m yr^{-1}) from Adsumilli et al. (2020) (**a**). Difference between observed basal melt rate from Adsumilli et al. (2020) and basal melt rate used for control simulation (observed - control) (m yr^{-1})(**b**). Also shown are zoomed in plots of observed melt rate minus average control melt rate for keys regions: the Filchner-Ronne ice shelf (**c**); the Totten glacier region (**d**); the Amundsen Sea Embayment (**e**); the Ross ice shelf (**f**) and Dronning Maud Land coast ice shelves (**g**). Bounding box colours for subplots **c** - **g** correspond to box locations outlined in **b**. Solid black contours on **b** - **g** show 2015 grounding line position, and dashed black contours show shelf edge. Black horizontal lines are scale bars corresponding to 100 km.

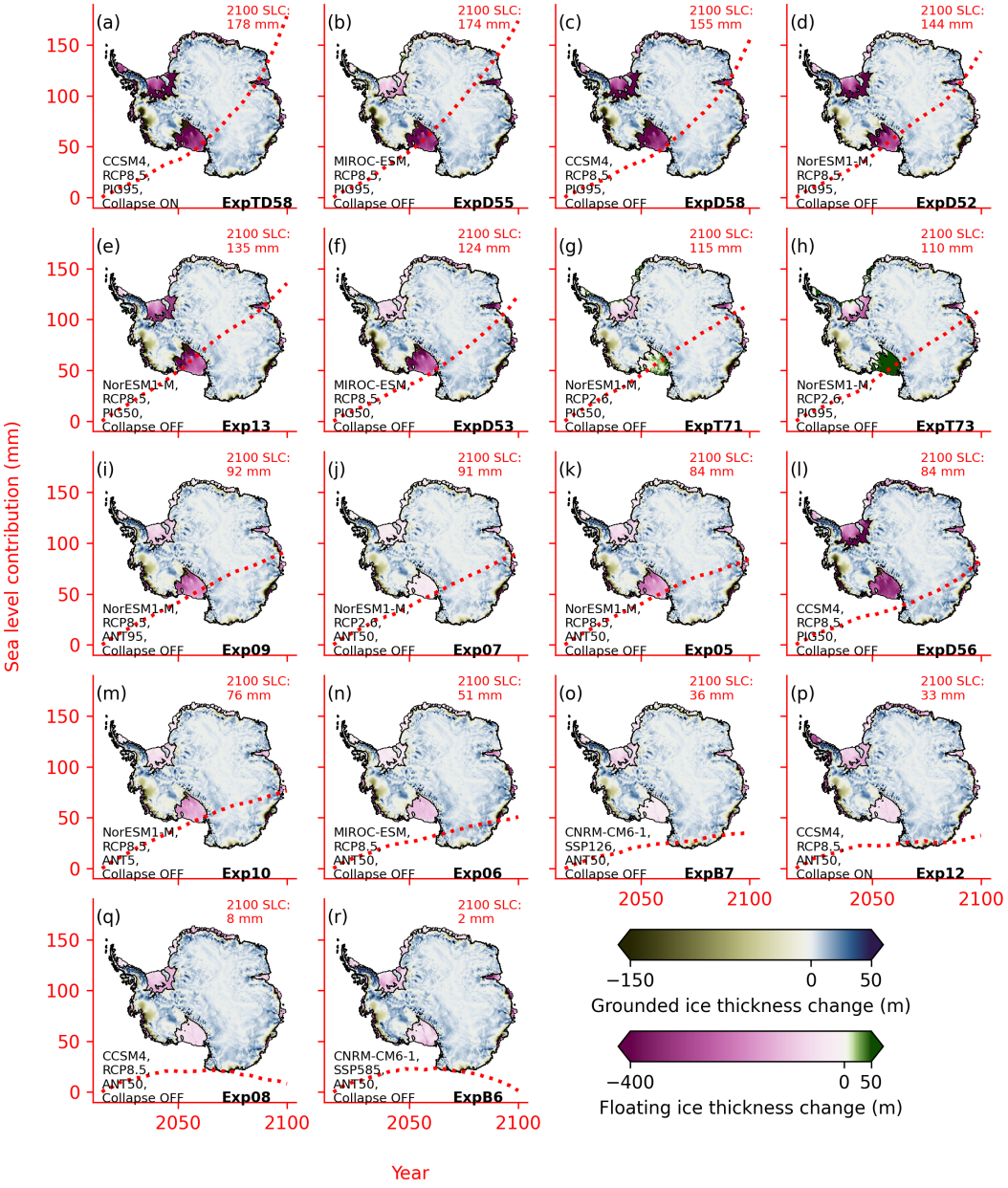

Fig. S5. Thickness change at 2100 relative to 2015 for all experiments, ordered by sea level contribution. Red dashed line shows sea level contribution from 2015 until 2100 to give an indication of rate and magnitude of mass loss. Black bold text corresponds to experiment number in Table 2 of the main text. Note use of seperate color schemes for grounded and floating ice.

Experiment	WAIS	EAIS	AP	1	2	3	4	5	6	7	8	9	10	11	12	13	14	15	16
5	52.52	29.4	2.26	8.64	-1.95	-8.42	8.59	38.16	6.19	-1.77	-2.16	17.26	31.89	4.75	5.12	-0.31	-2.53	-19.93	0.66
6	51.55	-8.61	8.08	6.07	-1.2	-10.46	6.7	14.27	0.49	-2.71	-14.64	15.36	32.14	7.34	9.76	-0.6	-1.01	-14.28	3.82
7	46.87	39.95	3.81	9.57	1.59	-7.84	8.96	35.99	7.03	-0.7	-12.63	15.66	31.47	5.53	6.61	-0.77	-1.99	-10.38	2.55
8	39.19	-31.5	0.53	3.97	-6.23	-9.75	4.65	8.93	-0.46	-3.51	-18.56	12.9	32.19	5.44	3.68	-0.45	-2.69	-20.41	-1.44
9	55.45	34.24	2.29	8.57	-1.94	-8.04	9.6	40.68	6.59	-1.67	-0.17	17.63	32.5	4.8	5.18	-0.31	-2.55	-19.53	0.66
10	49.51	24.77	2.12	8.61	-2.0	-8.72	7.81	35.47	5.86	-1.78	-3.88	16.87	31.16	4.66	5.0	-0.32	-2.53	-20.47	0.69
12	44.85	-25.46	13.14	4.08	-5.71	-9.73	4.88	13.13	-0.31	-2.77	-18.37	14.38	32.68	8.87	13.82	0.7	-1.38	-20.32	-1.43
13	71.57	61.59	2.34	8.99	-2.62	-4.25	15.09	52.4	8.31	-1.22	13.49	17.8	35.75	4.67	5.03	-0.1	-2.59	-15.07	-0.17
D52	76.1	64.82	3.01	9.64	-3.4	-0.55	15.7	48.37	7.18	-0.44	5.77	15.47	37.93	4.89	5.76	-0.09	-2.63	0.95	-0.59
D53	80.06	36.37	7.52	7.6	-1.29	-5.08	19.11	33.36	2.01	-1.02	-5.84	17.9	47.66	7.76	8.89	-0.4	-0.9	-9.77	3.97
D55	102.51	62.74	8.47	8.82	-1.55	-0.27	27.93	40.28	2.82	0.01	-3.8	19.28	62.16	7.07	9.64	-0.1	-0.99	-1.64	4.07
D56	83.21	0.96	-0.48	8.57	-7.07	-7.74	9.17	17.78	2.59	-2.67	-6.56	15.75	47.65	5.38	2.36	-0.15	-2.68	2.6	-1.27
D58	134.02	21.34	-0.32	9.91	-7.21	-5.14	12.17	20.23	2.26	-1.65	9.06	14.62	61.7	5.83	2.33	-0.07	-2.57	35.1	-1.53
T71	47.81	63.73	3.05	9.18	1.17	-3.71	14.78	49.79	9.16	-0.8	-14.77	14.99	34.31	5.32	5.96	-0.82	-2.05	-9.34	1.43
T73	42.82	63.34	3.7	8.94	0.32	0.65	16.47	44.86	8.86	-0.69	-17.64	13.01	33.41	5.48	6.39	-0.63	-2.02	-8.43	0.91
TD58	139.1	26.43	12.9	10.1	-6.68	-5.21	12.62	23.48	2.58	-1.25	9.04	15.8	62.02	9.31	13.61	0.65	-1.35	35.25	-1.54
B6	14.76	-10.34	-2.89	5.21	-0.79	-7.95	10.05	13.69	3.4	-2.59	-25.58	8.97	21.38	3.92	2.93	-2.25	-3.58	-24.31	-0.91
B7	25.4	9.04	1.28	8.73	2.43	-8.12	9.13	13.72	4.13	-1.58	-22.17	10.78	25.36	4.93	5.12	-1.2	-2.64	-15.57	2.72
control	36.46	13.05	3.51	11.21	2.98	-7.22	6.08	9.7	5.13	-1.13	-14.41	13.05	26.11	5.28	6.55	-1.05	-1.95	-11.0	3.7

Table S1. Masked sea level contribution in mm for WAIS, EAIS, and AP, as well as sectoral contributions for the 16 drainage basins detailed in the main text. Basins numbers correspond to: 1: Dronning Maud Land; 2: Enderby Land; 3: Lambert Glacier catchment; 4: Wilhelm II land; 5: Totten Sector; 6: George V Land; 7: Oates Land; 8: Ross Ice Shelf; 9: Getz ice shelf sector; 10: Amundsen Sea Embayment sector; 11: Abbott ice shelf sector; 12: George VI ice shelf sector; 13: Larsen sector; 14: Palmer Land; 15: Filchner-Ronne sector; 16: Brunt ice shelf sector. See Fig. 8 in main text.

References

Adusumilli, S., Fricker, H. A., Medley, B., Padman, L., and Siegfried, M. R.: Interannual variations in meltwater input to the Southern Ocean from Antarctic ice shelves, Nature Geoscience, 13, 616–620, https://doi.org/10.1038/s41561-020-0616-z, 2020.

Arthern, R. J., Winebrenner, D. P., and Vaughan, D. G.: Antarctic snow accumulation mapped using polarization of 4.3-cm wavelength microwave emission, Journal of Geophysical Research: Atmospheres, 111, https://doi.org/10.1029/2004JD005667, 2006.

Cornford, S. L., Martin, D. F., Graves, D. T., Ranken, D. F., Le Brocq, A. M., Gladstone, R. M., Payne, A. J., Ng, E. G., and Lipscomb, W. H.: Adaptive mesh, finite volume modeling of marine ice sheets, Journal of Computational Physics, 232, 529–549, https://doi.org/10.1016/j.jcp.2012.08.037, 2013.

Cornford, S. L., Martin, D. F., Payne, A. J., Ng, E. G., Le Brocq, A. M., Gladstone, R. M., Edwards, T. L., Shannon, S. R., Agosta, C., van den Broeke, M. R., Hellmer, H. H., Krinner, G., Ligtenberg, S. R. M., Timmermann, R., and Vaughan, D. G.: Century-scale simulations of the response of the West Antarctic Ice Sheet to a warming climate, The Cryosphere, 9, 1579–1600, https://doi.org/10.5194/tc-9-1579-2015, 2015.

Fretwell, P., Pritchard, H. D., Vaughan, D. G., Bamber, J. L., Barrand, N. E., Bell, R., Bianchi, C., Bingham, R. G., Blankenship, D. D., Casassa, G., Catania, G., Callens, D., Conway, H., Cook, A. J., Corr, H. F. J., Damaske, D., Damm, V., Ferraccioli, F., Forsberg, R., Fujita, S., Gim, Y., Gogineni, P., Griggs, J. A., Hindmarsh, R. C. A., Holmlund, P., Holt, J. W., Jacobel, R. W., Jenkins, A., Jokat, W., Jordan, T., King, E. C., Kohler, J., Krabill, W., Riger-Kusk, M., Langley, K. A., Leitchenkov, G., Leuschen, C., Luyendyk, B. P., Matsuoka, K., Mouginot, J., Nitsche, F. O., Nogi, Y., Nost, O. A., Popov, S. V., Rignot, E., Rippin, D. M., Rivera, A., Roberts, J., Ross, N., Siegert, M. J., Smith, A. M., Steinhage, D., Studinger, M., Sun, B., Tinto, B. K., Welch, B. C., Wilson, D., Young, D. A., Xiangbin, C., and Zirizzotti, A.: Bedmap2: improved ice bed, surface and thickness datasets for Antarctica, The Cryosphere, 7, 375–393, https://doi.org/10.5194/tc-7-375-2013, publisher: Copernicus GmbH, 2013.

Hooke, R.: Flow law for polycrystalline ice in glaciers: Comparison of theoretical predictions, laboratory data, and field measurements, Reviews of Geophysics, 19, 664–672, https://doi.org/10.1029/RG019i004p00664, _eprint: https://onlinelibrary.wiley.com/doi/pdf/10.1029/RG019i004p00664, 1981.

Mottram, R., Hansen, N., Kittel, C., van Wessem, J. M., Agosta, C., Amory, C., Boberg, F., van de Berg, W. J., Fettweis, X., Gossart, A., van Lipzig, N. P. M., van Meijgaard, E., Orr, A., Phillips, T., Webster, S., Simonsen, S. B., and Souverijns, N.: What is the surface mass balance of Antarctica? An intercomparison of regional climate model estimates, The Cryosphere, 15, 3751–3784, https://doi.org/10.5194/tc-15-3751-2021, publisher: Copernicus GmbH, 2021.

Rignot, E., Mouginot, J., and Scheuchl, B.: MEaSUREs InSAR-Based Antarctica Ice Velocity Map. (NSIDC-0484, Version 2), https://doi.org/https://doi.org/10.5067/D7GK8F5J8M8R., 2017.

Seroussi, H., Nowicki, S., Simon, E., Abe-Ouchi, A., Albrecht, T., Brondex, J., Cornford, S., Dumas, C., Gillet-Chaulet, F., Goelzer, H., Golledge, N. R., Gregory, J. M., Greve, R., Hoffman, M. J., Humbert, A., Huybrechts, P., Kleiner, T., Larour, E., Leguy, G., Lipscomb, W. H., Lowry, D., Mengel, M., Morlighem, M., Pattyn, F., Payne, A. J., Pollard, D., Price, S. F., Quiquet, A., Reerink, T. J., Reese, R., Rodehacke, C. B., Schlegel, N.-J., Shepherd, A., Sun, S., Sutter, J., Van Breedam, J., van de Wal, R. S. W., Winkelmann, R., and Zhang, T.: initMIP-Antarctica: an ice sheet model initialization experiment of ISMIP6, The Cryosphere, 13, 1441–1471, https://doi.org/10.5194/tc-13-1441-2019, 2019.

Tsai, V. C., Stewart, A. L., and Thompson, A. F.: Marine ice-sheet profiles and stability under Coulomb basal conditions, Journal of Glaciology, 61, 205–215, https://doi.org/10.3189/2015JoG14J221, 2015.